STUDY ON TEMPERATURE FIELD OF THERMAL CRACKING DRILLING FLOW FIELD UNDER THE CONDITION OF BOTTOM HOLE SUBMERGED JET

by

Guohua WANG[a*], Jun TAN[b], and Chengxiao LI[c]

[a] College of Petroleum and Natural Gas Engineering,
Southwest Petroleum University, Chengdu, China
[b] College of Petroleum Engineering,
Guangdong University of Petrochemical Technology, Maoming, China
[c] Drilling and Production Technology Research Institute of CNPC Chuanqing Drilling Engineering Co. Ltd., Guanghan, China

Original scientific paper
https://doi.org/10.2298/TSCI200605310W

In the deep well bottom hole environment, there are several different substances in the process of pyrolysis drilling, such as high temperature supercritical jet medium, cooling water and cuttings, which can be considered as submerged non-free jet of supercritical fluid in low temperature environment. From the energy point of view, there are heat transfer between supercritical fluid and cooling water, heat transfer between supercritical fluid and bottom rock surface, and heat transfer between up flow and well wall. Due to the complexity of the components, the transfer process of these energies is very complex, which has an important impact on the efficiency of thermal cracking drilling. Therefore, it is of great significance to study the heat transfer law under the condition of bottom hole submergence.

Key words: *temperature field, thermal cracking, submerged jet*

Introduction

The rock breaking method based on thermal jet is a kind of drilling method with wide application prospect in hard and brittle formation [1]. At present, the realization of this method is different pipe-lines are set in the drill pipe, and fuel, oxygen and water are injected into the downhole along different pipe-lines, and the injected mixture is ignited in the bottom hole reaction chamber to make the fuel react with oxygen, resulting in high temperature and high pressure environment; in this environment, water will be in supercritical state ($t \geq 375$ °C, $P \geq 22.1$ MPa) [2]. In this way, not only can the reaction rate of fuel and oxygen be accelerated, but also a high temperature medium composed of supercritical water and CO_2 can be formed. After the impact of thermal jet, a large amount of heat energy is transferred to the rock by the high temperature fluid, and the non-uniform expansion thermal stress is generated inside the rock, which promotes the formation of micro-cracks and continuous expansion of rock, and continuous heating conditions The thermal cracking and crushing of rock can be realized [3], as shown in fig. 1 [4].

* Corresponding author, e-mail: wangguohua@swpu.edu.cn

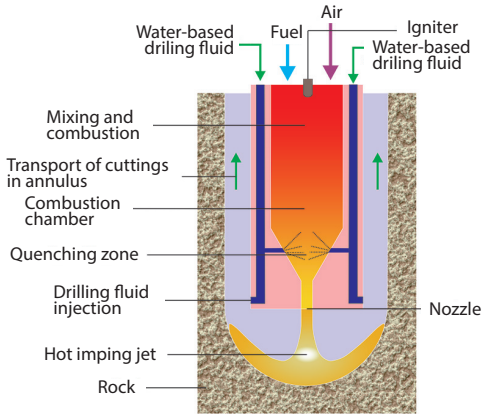

Figure 1. Schematic diagram of rock breaking process by thermal cracking

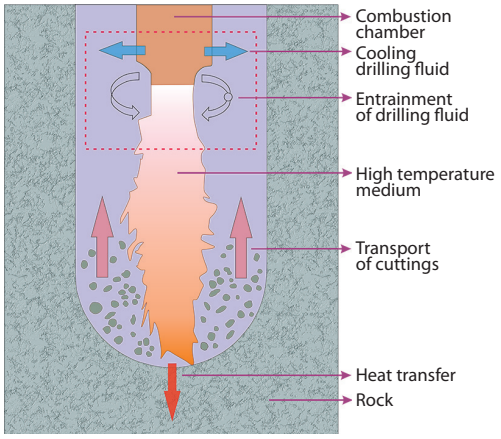

Figure 2. bottom hole environment of pyrolysis drilling

In the deep well bottom environment, as shown in fig. 2 [4], there are several different substances, such as high temperature supercritical jet medium, cooling water and rock cuttings, which can be regarded as submerged non-free jet of supercritical fluid in low temperature environment. From the energy point of view, there are heat transfer between supercritical fluid and cooling water, heat transfer between supercritical fluid and bottom rock surface, and heat transfer between up flow and well wall. Due to the complexity of the components, the transfer process of these energies is very complex, which has an important impact on the efficiency of thermal cracking drilling. Therefore, it is of great significance to study the heat transfer law under the condition of well bottom submergence.

Establishment of mathematical model

As shown in fig. 2, the governing equations which follow the law of conservation of mass, law of momentum, and law of conservation of energy are established by using the method of computational fluid dynamics:

$$\frac{\partial \rho}{\partial t}+\frac{\partial}{\partial x_i}\left(\rho u_i\right)=0 \tag{1}$$

$$\frac{\partial\left(\rho u_i\right)}{\partial t}+\frac{\partial}{\partial x_i}\left(\rho u_i u_j\right)=-\frac{\partial P}{\partial x_i}+\frac{\partial \tau_{ij}}{\partial x_j}+\rho g_i+F_i \tag{2}$$

$$\frac{\partial}{\partial x_j}\left(\rho h u_j\right)=u_i\frac{\partial P}{\partial x_i}+\tau_{ij}\frac{\partial u_i}{\partial x_j}+\frac{\partial}{\partial x_j}\left|\left(\frac{\mu}{\mathrm{Pr}}+\frac{\mu_t}{\mathrm{Pr}_t}\right)\frac{\partial h}{\partial x_j}\right| \tag{3}$$

for the aforementioned formula, the realizable κ-ε turbulence model is generally used to calculate and solve the previous formula [5, 6], so it is necessary to introduce the κ equation and the equation:

$$\frac{\partial\left(\rho k u_i\right)}{\partial x_i}=\frac{\partial}{\partial x_j}\left(a_k \mu_{\mathrm{eff}}\frac{\partial k}{\partial x_j}\right)+G_k-\rho\varepsilon \tag{4}$$

$$\frac{\partial\left(\rho\varepsilon u_i\right)}{\partial x_i}=\frac{\partial}{\partial x_j}\left(a_\varepsilon \mu_{\mathrm{eff}}\frac{\partial \varepsilon}{\partial x_j}\right)+\frac{C_{1\varepsilon}^{*}\varepsilon}{k}G_k-C_{2\varepsilon}\rho\frac{\varepsilon^2}{k} \tag{5}$$

in eqs. (4) and (5), the calculation method of constant and variable is [7]:

$$G_k=\mu_t\left[\left(\frac{\partial u_i}{\partial x_i}+\frac{\partial u_j}{\partial x_j}\right)\frac{\partial u_i}{\partial x_j}\right] \tag{6}$$

$$\mu_t = \rho C_\mu \frac{k^2}{\varepsilon} \tag{7}$$

$$C_{1\varepsilon}^* = C_{1\varepsilon} - \frac{\eta\left(1-\frac{\eta}{\eta_0}\right)}{1+\beta\eta^2} \tag{8}$$

$$\eta = \left(2E_{ij}E_{ij}\right)^{1/2}\frac{k}{\varepsilon} \tag{9}$$

$$E_{ij} = \frac{1}{2}\left(\frac{\partial u_i}{\partial x_j} + \frac{\partial u_j}{\partial x_i}\right) \tag{10}$$

$$C_\mu = 0.0845,\ C_{1\varepsilon} = 1.42,\ C_{2\varepsilon} = 1.68,\ a_k = a_\varepsilon = 1.39,\ \eta_0 = 4.377,\ \beta = 0.012 \tag{11}$$

Calculation area establishment

The calculation area as shown in fig. 3 is established, and the solid computing domain and fluid computing domain are set-up, respectively. The solid domain and fluid domain are connected by coupling surface, in which the coupling surface is the red surface shown in fig. 3. The coupling surface not only transfers heat but also transmits the pressure generated by the jet. The outer part of the calculation area is solid domain, and the inner part is fluid domain; the central nozzle is a thermal jet nozzle with a diameter of 5 mm; a cooling water nozzle with a diameter of 3 mm is set at the side; the borehole diameter is 50.8 mm, the diameter of the running pipe is 25.4 mm, and the distance from the central nozzle to the bottom of the well is 40 mm. The whole calculation area is discretized by structured grid, and the boundary-layer grid is divided at the solid wall. In view of the bottom hole submerged jet environment, the length of the calculation domain is usually set to five times of its width, which can ensure the full development of the bottom hole flow field, not only can meet the requirements of calculation accuracy [8], but also can save the calculation cost and greatly improve the model calculation efficiency.

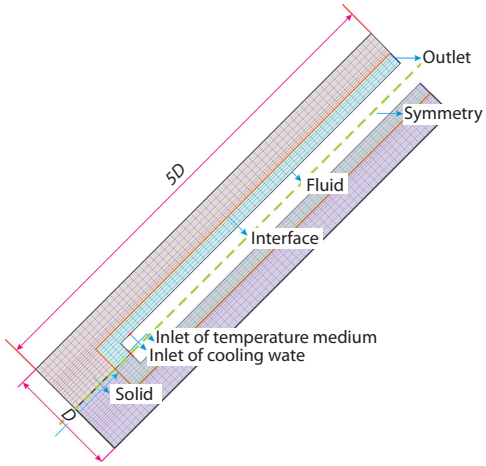

Figure 3. calculation area of pyrolysis drilling

There are three ways to deal with the heat transfer on the wall at the junction of fluid and solid. The first is to create a wall mesh with thickness in the solid domain in the preprocessing module and set it as the solid domain, as shown in fig. 4(a), which is the most realistic simulation method. The second method is to only set up the mesh in the fluid domain and specify a wall thickness on the solid domain, as shown in fig. 4(b), which can save the calculation cost, but its disadvantage is that only the normal heat conduction of the wall can be considered, which is deviated from the real situation. The third method is similar to the second method, but the shell conduction option is activated in the solid domain to create a single or multi-layer virtual grid, as shown in fig. 4(c). The limiting factor is that the simulation results can only view

the temperature of both sides and shell elements. In order to get closer to the real situation and obtain more detailed data, the wall heat transfer between the fluid domain and the solid domain is treated in the first way, so as to ensure the accurate simulation of the heat transfer effect carried by the high temperature jet medium on the rock surface and inside.

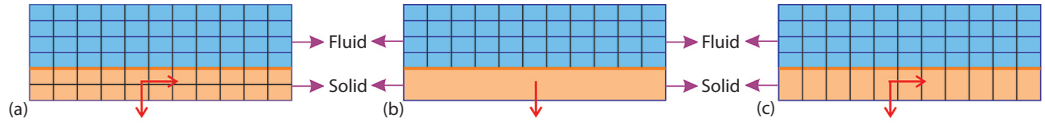

Figure 4. Heat transfer treatment of fluid solid boundary; (a) heat transferred in all directions, (b) heat transferred only vertical to the wall, and (c) heat transferred in all directions

For the solid domain, it can be set as the thermal physical properties of granite [9], with density of 2000 kg/m^3, specific heat capacity of 0.8 kJ/(kg°C), and heat conduction coefficient of 2.6 W/(m°C). On the other hand, the high temperature jet medium in the fluid domain is mainly composed of supercritical water and contains a small amount of combustion products, such as CO_2. Due to its low content, the existence of combustion products such as CO_2 can be ignored, and the physical properties of high temperature jet medium can be directly set as that of supercritical water. However, in the supercritical region ($T >$ PCT), the properties of high temperature medium tend to gas, however, the cooling drilling fluid around presents liquid properties [10, 11]. Therefore, the thermal physical properties such as density, viscosity, specific heat and heat conduction coefficient will change dramatically near the contact boundary between supercritical fluid and surrounding fluid. Therefore, in the bottom hole inundation environment, the thermal physical properties of water have an important impact on the numerical simulation results of bottom hole flow field, as shown in fig. 5. In view of the aforementioned situation, it can be considered that the thermal physical properties of supercritical water are mainly affected by the temperature change, while under the critical pressure (22.4 MPa), the influence of local pressure change on its thermophysical properties is generally ignored [12]. Based on the software RefProp 8.0, the change of material properties of water with temperature under critical pressure can be calculated, as shown in fig. 5 [13]. In order to ensure the calculation accuracy, each temperature interval is taken as 0.2 °C.

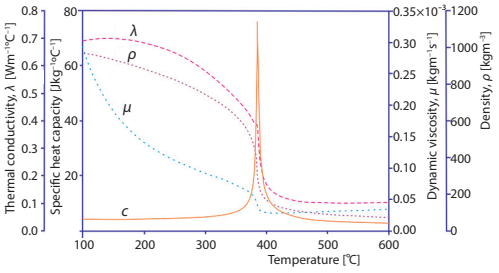

Figure 5. Thermophysical properties of supercritical water at 22.4 mpa

Since the bottom hole is in a high pressure state, but the temperature changes sharply, it can be considered that the physical properties of supercritical water are mainly affected by temperature, while the effect of pressure change is ignored [14, 15]. The data of thermophysical properties of supercritical water varying with temperature shown in fig. 5 are interpolated by Newton method, respectively. The principle is:

$$n_N(x) = a_0 + a_1(x - x_0) + a_2(x - x_0)(x - x_1) + \ldots + a_N(x - x_0)(x - x_1)\ldots(x - x_{N-1})$$
$$n_0(x) = a_0 \tag{12}$$

According to the previous equations, it can be obtained that the numerical coefficients of Newton interpolation satisfy the following equations:

$$a_0 = y_0,\ a_1 = \frac{y_1 - a_0}{x_1 - x_0} = \frac{y_1 - y_0}{x_1 - x_0} = Df_0,\ a_2 = \frac{\frac{y_2 - y_1}{x_{2-x_1}} \frac{y_1 - y_0}{x_1 - x_0}}{x_2 - x_0} = \frac{Df_1 - Df_0}{x_2 - x_0} = D^2 f$$
$$\cdots \tag{13}$$
$$a_{N-1} = \frac{D^{N-2} f_1 - D^{N-2} f_0}{x_{N-1} - x_0} = D^{N-1} f,\ a_N = \frac{D^{N-1} f_1 - D^{N-1} f_0}{x_N - x_0} = D^N f$$

Then, User-Defined Functions is used to program, so that the thermophysical properties of supercritical water with temperature can be invoked in the calculation process, so as to ensure the accuracy of the flow field calculation.

For the boundary conditions shown in fig. 3, since the physical properties of supercritical water change with temperature, the high temperature medium inlet is set as the pressure inlet boundary, with inlet pressure $P = 40$ MPa and temperature $T = 600$ °C. The cooling water inlet is set as mass-flow boundary, $q = 0.15$ kg/s, temperature $T = 20$ °C. The direction is inlet normal and an outlet boundary is set in the whole calculation domain, and all fluids-flow from the annulus. The results show that the pressure outlet condition, $P = 22.4$ MPa. The symmetrical boundary condition is adopted for the wellbore axis. The heat transfer effect of fluid to surrounding rock is considered in the whole flow process, so the fluid solid interface is set as the coupled heat transfer mode. The smooth wall without sliding is adopted for the wall condition, and the single-layer wall function is used to modify u near the well wall:

$$y^+ = \frac{\rho C_\mu^{1/4} K^{1/2}}{\mu} \tag{14}$$

when $y^+ < 11.5, \mu_{\text{eff}} = \mu$, when $y^+ > 11.5, \mu_{\text{eff}} = \mu + \mu_t$.

Analysis of calculation results

Grid independence verification

In order to ensure the accuracy of the calculation results, the grid independence of the whole calculation area is verified. As shown in fig. 6, the whole calculation area is discretized by hexahedral structured grid, and the coupling interface is used to segment the solid domain and fluid domain. The convergence results can be obtained by setting the computational domain grid to different sizes. As can be seen from fig. 7, when the mesh size is less than 0.05 mm, the calculation results tend to be stable without any change. Considering the calculation accuracy and cost, the mesh size of the whole calculation domain is set as 0.05 mm.

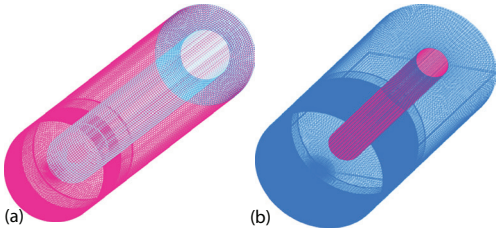

Figure 6. Grid diagram of coupling calculation of bottom hole submerged non-free jet; (a) fluid domain grid and (b) solid domain grid

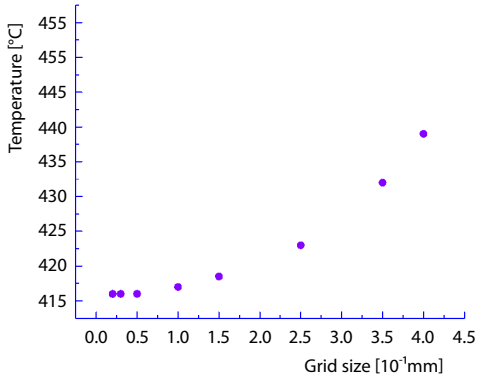

Figure 7. Schematic diagram of temperature calculation results changing with grid size

Analysis of flow field results

After calculation, when the flow field is stable, the cloud chart and streamline distribution diagram of thermal jet flow field at the

bottom hole as shown in fig. 8(b) can be obtained. It can be seen from the figure that under the condition of submerged jet at the bottom of the well, the jet medium will have strong entrainment with the surrounding fluid, and form a low speed eddy current area on both sides of the jet; after the jet reaches the bottom of the well, it overflows along the central axis of the jet to both sides of the well wall, and then returns along the well wall. More importantly, compared with fig. 8(a), compared with the ordinary high pressure jet, under the same inlet pressure (P = 40 MPa), setting the outlet temperature of thermal jet at 600 °C, it is obvious that the jet velocity of thermal jet is higher, and the thermal jet can keep the kinetic energy unchanged in a longer distance, that is, the attenuation degree of jet velocity along the jet center line is lower. Comparing figs. 8(c) and 8(d), it can be seen that the pressure distribution of thermal jet and conventional jet is also different on the bottom hole plane. It can be seen from fig. 8(c) that under the same inlet conditions, the pressure of conventional jet reaches 36 MPa, while that of thermal jet is only 28 MPa. This is because although the flow velocity of thermal jet is much higher than that of conventional jet, the jet medium is supercritical water, and its density rapidly decreases at high temperature, so the jet pressure becomes smaller.

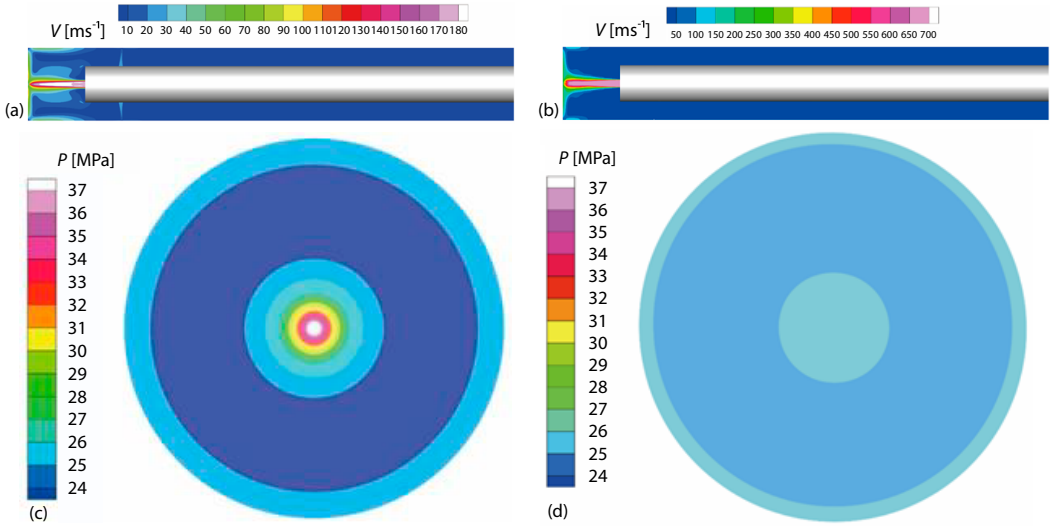

Figure 8. Comparison of bottom hole flow field of thermal jet and ordinary high pressure jet; (a) schematic diagram of bottom hole flow field of ordinary high pressure jet, (b) schematic diagram of bottom hole flow field of thermal jet, (c) bottom hole pressure distribution of conventional jet, and (d) bottom hole pressure distribution of thermal jet

Figure 9(a) shows the bottom hole temperature field nephogram of thermal jet. It can be seen from the figure that under the condition of submerged jet, due to the limitation of the surrounding fluid, when the high temperature medium of the jet is ejected from the nozzle, it will rapidly entrain the surrounding fluid and transfer heat to the surrounding fluid area. After that, the jet reaches the bottom of the hole along the axis of the nozzle, transfers heat to the rock surface, diffuses to both sides along the bottom plane, and finally returns along the well wall; during the upward return process, two lateral nozzles in the annulus inject cooling water into the annulus (the temperature is 20 °C), and the temperature in this area drops, and then the temperature remains almost unchanged. Therefore, by adjusting the cooling water flow rate of the two lateral nozzles, the high temperature area can be completely controlled at the bottom of the well without affecting the well wall. Figure 9(b) shows the temperature distribution of the bottom

hole rock during the thermal jet process. It can be seen from the figure that the temperature influence range is limited, the propagation in the rock matrix is very slow, and the temperature gradient is high.

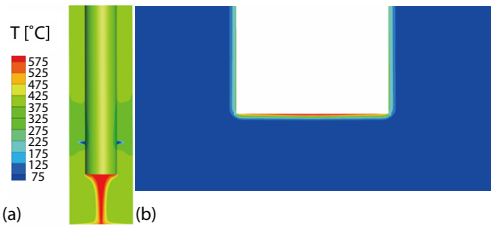

Figure 9. Bottom hole temperature field of thermal jet under submerged jet condition; (a) schematic diagram of temperature field in bottom hole fluid domain of thermal jet and (b) temperature field diagram of solid field in thermal jet well bottom, t = 1 second

Figure 10 shows the variation of various parameters in the thermal jet flow field with the injection distance. It can be seen from fig. 10(a) that the velocity of both thermal jet and conventional jet can maintain a fairly long velocity core along the jet distance, and the jet velocity is almost unchanged in this area. However, the velocity of thermal jet is higher, and the downward trend is slower than that of conventional jet. It can be seen from fig. 10(b) that the jet temperature is almost constant within the length of the jet distance, but the temperature decreases slightly when it is close to the bottom of the well due to heat exchange with the rock surface, while the variation trend of the jet medium density is opposite to that of the temperature.

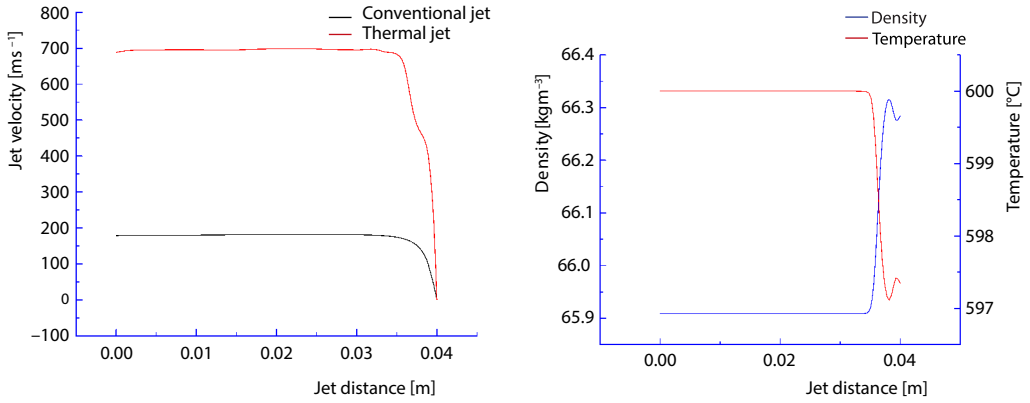

Figure 10. Variation of parameters in flow field with spray distance; (a) velocity attenuation of conventional jet and thermal jet along axial direction and (b) variation of jet medium temperature and density with jet distance

Figure 11. shows the distribution of jet pressure along the bottom of the well for both conventional and thermal jets. It can be seen from the figure that the pressure distribution of the two is similar, with the highest pressure at the central straight point; the jet pressure of the conventional jet is higher than that of the thermal jet; under the same inlet pressure (P = 40 MPa), the pressure of the conventional jet is higher than that of the thermal jet at the jet center point and well wall, which is caused by the much lower density of the thermal jet medium than that of the conventional jet.

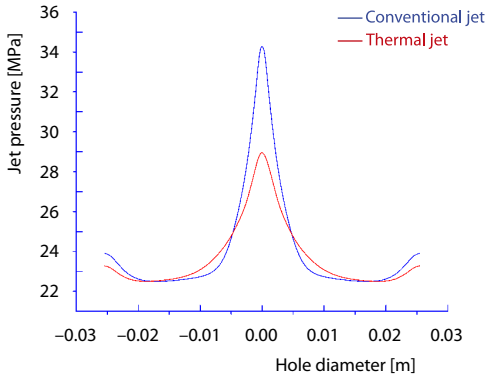

Figure 11. distribution of jet pressure along borehole diameter

Conclusion

- At the same inlet pressure, the jet velocity of thermal jet is higher than that of conventional jet, which can reach 712 m/s, while that of conventional jet is only 187 m/s.
- The density of thermal jet medium is very small at high temperature, so the jet impact force is lower, only about 26 MPa, but the conventional jet can reach 37 MPa.
- It can be seen from the figure that the temperature influence range is limited, the propagation in the rock matrix is very slow and the temperature gradient is high.

Nomenclature

$C_{1\varepsilon}$ – empirical constant, [–]
$C_{2\varepsilon}$ – empirical constant, [–]
h – enthalpy, [–]
P – pressure, [MPa]
Pr – Prandtl number, [–]
u_i – velocity vector component, [ms^{-1}]
u_t – effective viscosity, [mPa·s]

Greek symbols

μ – absolute viscosity, [mPa·s]
ρ – density, [kgm^{-3}]
τ_{ij} – viscous stress tensor, [–]

Reference

[1] Walsh, S. C., *et al*., Grain-Scale Failure in Thermal Spallation Drilling, *Proceedings*, Thirty-Seventh Workshop on Geothermal Reservoir Engineering Stanford University, Stanford, Cal., USA, 2012
[2] Wagner, W., The IAPWS Formulation 1995 for the Thermodynamic Properties of Ordinary Water Substance for General and Scientific Use, *Journal of Physical & Chemical Reference Data*, *31* (2002), 2, pp. 387-435
[3] Augustine, C. R., Hydrothermal Spallation Drilling and Advanced Energy Conversion Technologies for Engineered Geothermal Systems, Ph. D. thesis, Massachusetts Institute of Technology, Kambridge, Mass., USA, 2009
[4] Rothenfluh, T., Heat Transfer Phenomena of Supercritical Water Jets in Hydrothermal Spallation Drilling, Ph. D. thesis, ETH, Zurich, Switzerland, 2013
[5] Schuler, M. J., *et al*., Numerical Analysis of Penetration Lengths in Submerged Supercritical Water Jets, *Journal of Supercritical Fluids*, *82* (2013), Oct., pp. 213-220
[6] Pope, S., An Explanation of the Turbulent Round-Jet/Plane-Jet Anomaly, *AIAA Journal*, *16* (1978), 3, pp. 279-281
[7] Hu, K., *et al*., The CFD Simulation of Non-Free Submerged Water Jet, *China Petroleum Machinery*, *38* (2010), 11, pp. 41-44
[8] Moslemi, A., Ahmadi, G., Study of the Hydraulic Performance of Drill Bits Using a Computational Particle-Tracking Method, *Spe Drilling & Completion*, *29* (2014), 1, pp. 28-35
[9] Li, M., *et al*., Simulation of Thermal Stress Effects in Submerged Continuous Water Jets on the Optimal Standoff Distance during Rock Breaking, *Powder Technology*, *320* (2017), 123, pp. 47-59
[10] Wagner, W., The IAPWS Formulation 1995 for the Thermodynamic Properties of Ordinary Water Substance for General and Scientific Use, *Journal of Physical & Chemical Reference Data*, *31* (2002), 2, pp. 387-435
[11] Rothenfluh, T., *et al*., Penetration Length Studies of Supercritical Water Jets Submerged in a Subcritical Water Environment Using a Novel Optical Schlieren Method, *Journal of Supercritical Fluids*, *57* (2011), 2, pp. 175-182
[12] Schuler, M. J., *et al*., Simulation of the Thermal Field of Submerged Supercritical Water Jets at Near-Critical Pressures, *Journal of Supercritical Fluids*, *75* (2013), 3, pp. 128-137
[13] Lemmon, E., W., *et al*., The NIST Standard Reference Database 23: Reference Fluid Thermodynamic and Transport Properties – REFPROP, Gaithersburg, Md., USA, ed. 9.0, 2010
[14] Roelofs, F., The CFD Analyses of Heat Transfer to Supercritical Water Flowing Vertically Upward in A Tube, NRG Rapport No. 21353(04.60811), NRG, Arnhem, The Netherlands, 2004
[15] Song, X., *et al*., Numerical Analysis of the Impact Flow Field of Multi-Orifice Nozzle Hydrothermal Jet Combined with Cooling Water, *Int. Jou. of Heat & Mass Tra.*, *114* (2017), Nov., pp. 578-589

Paper submitted: June 5, 2020
Paper revised: August 27, 2020
Paper accepted: September 21, 2020